

Detectability of the 21 cm signal with BINGO through cross-correlation with photometric surveys

Gabriel A. S. Silva,^a Camila P. Novaes,^a Carlos A. Wuensche,^a Eduardo J. de Mericia,^a Bruno B. Bizarria,^{a,b} Jiajun Zhang,^{c,d} Elcio Abdalla,^{e,f,g} Filipe B. Abdalla,^{e,h,i,j} Amilcar R. Queiroz,^k Thyroso Villela,^{a,l,m} Bin Wang,^{n,o} Chang Feng,^{h,i,p} Edmar C. Gurjão,^q Alessandro Marins^h

^aInstituto Nacional de Pesquisas Espaciais,

Av. dos Astronautas 175, Jardim da Granja, São José dos Campos, SP, Brazil

^bJodrell Bank Centre for Astrophysics, University of Manchester,

Manchester M13 9PL, UK

^cShanghai Astronomical Observatory (SHAO), Nandan Road 80, Shanghai, 200030, China

^dState Key Laboratory of Radio Astronomy and Technology, 20A Datun Road, Chaoyang District, Beijing, 100101, China

^eInstituto de Física, Universidade de São Paulo,

C.P. 66.318, CEP 05315-970, São Paulo, Brazil

^fUniversidade Estadual da Paraíba,

Rua Baraúnas, 351, Bairro Universitário, Campina Grande, Brazil

^gDepartamento de Física, Centro de Ciências Exatas e da Natureza, Universidade Federal da Paraíba,

CEP 58059-970, João Pessoa, Brazil

^hDepartment of Astronomy, School of Physical Sciences, University of Science and Technology of China,

Hefei, Anhui 230026, China

ⁱSchool of Astronomy and Space Science, University of Science and Technology of China,

Hefei, Anhui 230026, China

^jDepartment of Physics and Electronics, Rhodes University,

PO Box 94, Grahamstown, 6140, South Africa

^kUnidade Acadêmica de Física, Univ. Federal de Campina Grande,

R. Aprígio Veloso, 58429-900 - Campina Grande, Brazil

^lCentro de Gestão e Estudos Estratégicos SCS Qd 9, Lote C, Torre C S/N Salas 401 a 405, 70308-200 - Brasília, DF, Brazil

^mInstituto de Física, Universidade de Brasília, Campus Universitário Darcy Ribeiro, 70910-900 - Brasília, DF, Brazil

¹Corresponding author.

ⁿCenter for Gravitation and Cosmology, Yangzhou University,
Yangzhou 224009, China

^oSchool of Aeronautics and Astronautics, Shanghai Jiao Tong University,
Shanghai 200240, China

^pCAS Key Laboratory for Research in Galaxies and Cosmology, University of Science and Technol-
ogy of China,
Hefei, Anhui 230026, China

^qDepartamento de Engenharia Elétrica, Univ. Federal de Campina Grande,
R. Aprígio Veloso, 58429-900 - Campina Grande, Brazil

E-mail: gabriel.souza@inpe.br

Abstract. 21 cm intensity mapping (HI IM) can efficiently survey large cosmic volumes with good redshift resolution, but systematics and foreground contamination pose major challenges for extracting precise cosmological information. Cross-correlation with galaxy surveys offers an efficient mitigation strategy, as the two datasets have largely uncorrelated systematics. We assess the detectability of the 21 cm signal from the BINGO radio telescope through cross-correlation with the LSST photometric survey, given their strong overlap in area and redshift. Using lognormal simulations, we model the cosmological signal in the BINGO frequency range (980–1260 MHz), incorporating thermal noise, foregrounds, and cleaning. LSST simulations include photometric redshift (photo- z) uncertainties and galaxy number density in the first three redshift bins ($\bar{z} \approx 0.25, 0.35, 0.45$), matching expected performance after 10 years of the survey. We show that photo- z errors significantly increase noise in the cross-correlation, reducing its statistical significance to levels comparable with the autocorrelation. Still, the HI signal remains detectable through cross-correlation, even with LSST-like photo- z uncertainties. Our results support the viability of this approach under realistic conditions and motivate further refinement of current analysis methods.

KEYWORDS: Cosmological simulations, redshift surveys, power spectrum.

Contents

1	Introduction	1
2	Angular power spectrum: theoretical modeling and measurement	3
2.1	Auto- and cross-correlation modeling	3
2.2	Angular power spectrum calculation	4
3	Synthetic data	4
3.1	H _I intensity mapping simulation	5
3.1.1	Cosmological signal	5
3.1.2	Sky coverage, instrumental effects and foreground signals	5
3.2	Photometric galaxy catalog simulation	6
4	H_I signal detection	7
4.1	Foreground cleaning	7
4.2	Results	9
4.2.1	Angular power spectrum estimation	10
4.2.2	Statistical Significance	14
5	Parameter estimation	16
6	Summary and conclusions	19

1 Introduction

The mapping of the distribution of the luminous matter has significantly contributed to our knowledge of the contents and evolution of the Universe’s large-scale structure, while corroborating the validity of the standard Λ CDM model. However, even with excellent agreement with many observations, the Λ CDM model still fails in explaining most of the Universe’s content, the so-called dark matter and dark energy. Motivated by the necessity of understanding the physical nature of these components, as well as addressing and explaining many other open questions in cosmology, a next generation of experiments is expected to perform cosmological measurements with unprecedented accuracy. Examples of these experiments are the James Webb Space Telescope (e.g., [1]), the Euclid satellite (e.g., [2]), and the Vera C. Rubin Observatory’s Legacy Survey of Space and Time - LSST (e.g., [3]), which surveys the galaxy distribution of the Universe through photometric and spectroscopic measurements in the optical and near-infrared spectra.

As an alternative, we have also been using radio wavelengths to measure the clustering of galaxies through the redshifted 21 cm emission resulting from the hyperfine transition line of neutral hydrogen (H_I). In particular, the intensity mapping (IM) of the 21 cm signal has emerged as a promising way to map the three-dimensional distribution of structures in the Universe. Among the forthcoming 21 cm intensity mapping instruments, we can mention Tianlai¹ [4], HIRAX [5], the Five-Hundred-Meter Aperture Spherical Radio Telescope [FAST; 6], the Square Kilometer Array

¹http://tianlai.bao.ac.cn/wiki/index.php/Main_Page

Observatory² [SKAO; 7], and the Baryon Acoustic Oscillations from Integrated Neutral Gas Observations³ [BINGO; 8–10]. While observations are already being conducted by, e.g., MeerKAT⁴ [11], a pathfinder survey and precursor of SKAO, and the Canadian Hydrogen Intensity Mapping Experiment⁵ [CHIME; 12].

Measuring the 21 cm signal from galaxy clustering is a challenging task. The presence of strong galactic emission, with synchrotron radiation being the most intense component, along with the existence of extragalactic sources (both unresolved and resolved), act as foregrounds for 21 cm observations [8]. Separating these different components and extracting the desired cosmological signal is a crucial step, with many methods developed to recover the 21 cm signal [13–16]. Nevertheless, even when well reconstructed, the foreground-cleaned maps still contain residual contamination and a loss of the cosmological signal. Furthermore, systematic effects are also important sources of contamination, including thermal noise [8, 17], $1/f$ noise [18, 19], radio frequency interference, beam modeling [20], and calibration errors [21]. A way of mitigating such effects on power spectrum estimations and increasing the signal-to-noise ratio (SNR) is to estimate the cross-correlation signal between the foreground cleaned maps and galaxy catalogs, as the systematics and contaminant signal from the two datasets are uncorrelated. In fact, most of the power spectrum detection so far have been achieved via cross-correlation [22–27], with a claim of detection of the autocorrelation from interferometric observations by [28].

Current correlated clustering studies, as reported above, rely on the use of power spectrum estimators in the Fourier space, given that the small surveyed areas (typically less than a few hundred deg^2 [29–31]) allow the resampling of pixelized maps onto a Cartesian grid without accounting for wide-angle effects like non-parallelism on the line-of-sights for $\ell \gtrsim 100$ [32–34]. Recently, [27] reported a detection of the 21 cm signal using a stacking approach, averaging the 21 cm maps at the locations of the objects in a galaxy catalog. To our knowledge, no detection was reported so far in the harmonic space, which has been less explored in this context.

The analysis using the angular power spectrum has been employed primarily for Fisher matrix analyses, as in [35–37], where the authors forecasts astrophysical and cosmological parameters using auto- and cross-correlations of 21 cm and other surveys. Less commonly, [38] employ synthetic data to study the correlation between 21 cm map and a galaxy survey. Regardless of the estimator, detections of the H I signal through cross-correlation analyses have been performed using spectroscopic galaxy surveys, owing to their more precise redshift determination. In fact, most studies in the literature, including those based on simulations, follow this approach. An exception is presented by [39], which investigates how the redshift uncertainty impacts the cross-correlation signal when using photometric surveys.

Previous work has highlighted the limitations of cross-correlation between H I IM and photometric galaxy catalogs, such as difficulties in modeling the accurate selection function and the effect of smearing the signal in the line-of-sight direction, which produces a loss in the amplitude of the correlation signal [39]. However, due to the great possibilities that arise from current and future photometric galaxy surveys like the Dark Energy Survey (DES) [40], LSST / Rubin Observatory [3], Javalambre Physics of the Accelerating Universe Astrophysical Survey (J-PAS) [41], Subaru Hyper Suprime-Cam (HSC) [42] and Physics of the Accelerating Universe (PAU) Survey [43], it is important to develop the literature with quantitative analyses of this type of correlation. Furthermore, the use of the angular power spectrum (APS; C_ℓ) is especially well suited for these analyses, as it

²<https://www.skatelescope.org/>

³<https://www.bingotelescope.org/en/>

⁴<https://www.ska.ac.za/science-engineering/meerkat>

⁵<https://chime-experiment.ca/>

naturally incorporates all the information within a given redshift bin and remains robust against photometric redshift (photo- z) errors, in contrast with three-dimensional $P(k)$ approaches that require accurate radial positions.

In this paper, we focus on the use of synthetic data in the harmonic space, to investigate the synergy between future observations conducted by the BINGO radio telescope and the LSST photometric galaxy survey. We chose the LSST survey as our case study, mainly motivated by its large overlap in area (the entire BINGO sky coverage, $\sim 5000\text{deg}^2$) and redshift with BINGO. Notice that, unlike [39], where the galaxy sample is selected by matching the redshift range of the H I survey, we consider the entire photo- z bin, that is, a broader redshift distribution of galaxies. To our knowledge, this approach has only been partially explored through Fisher matrix forecasts, as in [36]. Here, we assess the detectability of the 21 cm signal through the cross-correlation of future BINGO and LSST observations, and investigate the impact of photo- z uncertainties, as well as the presence of foreground contaminants, on such analyses.

This paper is organized as follows: Section 2 present the theoretical modeling of the APS for auto and cross-correlation and how they are measured from simulations; Section 3 describes our synthetic data sets, simulating BINGO and LSST surveys; Section 4 presents the foreground cleaning method applied to BINGO simulations and evaluates the statistical significance of an H I detection through auto and cross-correlation; studies of how well astrophysical parameters describing the H I signal would be constrained are summarized in Section 5; we conclude in Section 6.

2 Angular power spectrum: theoretical modeling and measurement

2.1 Auto- and cross-correlation modeling

In this work, auto-correlation always refers to H I -H I correlations, and cross-correlations always refer to H I -Galaxies correlations. Let $\delta_X(\mathbf{k})$ denote the Fourier transform of observed overdensity fluctuation of a tracer X of the matter field inside some volume of Universe. It can be modeled in terms of the underlying dark matter distribution at $z = 0$, $\delta(\mathbf{k}, 0)$, as a function of the \mathbf{k} modes and redshift z [44],

$$\delta_X(\mathbf{k}, z) = b_X(\mathbf{k}, z)D(z)\delta(\mathbf{k}, 0), \quad (2.1)$$

where b_X the bias term and $D(z)$ is the growth function. The power spectrum, $P_{XY}(k, z)$, is such that,

$$\langle \delta_X(\mathbf{k}, z)\delta_Y^*(\mathbf{k}', z) \rangle = (2\pi)^3 \delta^D(\mathbf{k} - \mathbf{k}') P_{XY}(k, z), \quad (2.2)$$

where δ^D is the Dirac delta function. The indexes X, Y represent the biased matter tracers, with $X = Y$ for the auto-power spectrum, and $X \neq Y$, for the cross power spectrum. It can be written as a function of the matter power spectrum at $z = 0$, $P(k)$, as $P_{XY}(k, z) = b_X b_Y r D^2(z) P(k)$, where r is the correlation coefficient, accounting for the stochasticity between the two fields [25, 26, 45].

In this work, $X = \text{H}\text{I}$ and $Y = g$ (galaxy survey). Projecting their three-dimensional distributions (Equation 2.1) on the sky by integrating them along the line of sight $\hat{\mathbf{n}}$, leads to

$$\delta_g(\hat{\mathbf{n}}) = \int dz \delta_g(\chi(z)\hat{\mathbf{n}}, z)n(z), \quad (2.3a)$$

$$\delta_{\text{H}\text{I}}(\hat{\mathbf{n}}) = \int dz \delta_{\text{H}\text{I}}(\chi(z)\hat{\mathbf{n}}, z)\phi(z)\bar{T}_{\text{H}\text{I}}, \quad (2.3b)$$

where $\chi(z)$ is the comoving distance to redshift z , $n(z)$ is the galaxy normalized redshift distribution, $\phi(z)$ is the projection kernel for H I IM⁶. The average brightness temperature of the 21 cm emission

⁶We consider a top-hat kernel where, for a BINGO redshift bin i , $\phi(z) = 1/(z_{i,\text{max}} - z_{i,\text{min}})$ for $z_{i,\text{min}} < z < z_{i,\text{max}}$ and $\phi(z) = 0$ otherwise.

can be written as $\bar{T}_{\text{HI}} = 188 h \Omega_{\text{HI}}(z) [(1+z)^2/E(z)] \text{ mK}$ [8], where $E(z) = H(z)/H_0$ is the normalized Hubble parameter, $H_0 = 100 h \text{ km s}^{-1} \text{ Mpc}^{-1}$, and Ω_{HI} is the HI dimensionless density parameter.

Decomposing the projected signal in spherical harmonics [29], we have

$$\delta_X(\hat{\mathbf{n}}) = \sum_{\ell=0}^{\infty} \sum_{m=-\ell}^{\ell} a_{\ell m} Y_{\ell m}, \quad (2.4)$$

where $a_{\ell m}$ are the coefficients and $Y_{\ell m}$ the harmonic functions. The $a_{\ell m}$'s are related to the overdensity through $a_{\ell m}^X = \int d\Omega \delta_X(\hat{\mathbf{n}}) Y_{\ell m}(\hat{\mathbf{n}})$. Following [44, 46], the coefficients can be written as

$$a_{\ell m}^X = \frac{4\pi i^\ell}{(2\pi)^3} \int d^3k W_{X,\ell}^i(k) \delta(\mathbf{k}, 0) Y_{\ell m}(\hat{\mathbf{k}}), \quad (2.5)$$

with the redshift dependence gathered in the window function

$$W_{X,\ell}^i(k) = \int dz b_X(z) \phi'(z) D(z) j_\ell(k\chi(z)) \quad (2.6)$$

where $\phi'(z) = n(z)$, for $X = g$, and $\phi'(z) = \phi(z) \bar{T}_{\text{HI}}$, for $X = \text{HI}$; j_ℓ is the spherical Bessel function. Therefore, the APS can be written as a function of the matter power spectrum

$$\begin{aligned} C_{XY,\ell}^{ij} &\equiv \langle a_{X,\ell m}^i a_{Y,\ell m}^{j*} \rangle \\ &= \int dk k^2 W_{X,\ell}^i(k) W_{Y,\ell}^j(k) P(k), \end{aligned} \quad (2.7)$$

where the indices i, j denote the tomographic redshift bins.

The theoretical APS used in this paper, for auto- ($i = j$ and $X = Y$) and cross-correlations ($i \neq j$, for the same tracer, $X = Y$, or for different tracers, $X \neq Y$), were computed using the Unified Cosmological Library for C_ℓ (UCLC ℓ) code [44, 47]. UCLC ℓ calculates the APS by integrating the HI projection kernel $\phi(z)$ and the galaxy redshift distribution $n(z)$, as described in Equations 2.6 and 2.7. It employs the clustering information from the model power spectrum $P(k)$ as computed with the CLASS Boltzmann code [48, 49]. We account for the non-linear evolution of the Universe as well as the impact of redshift-space distortion effect, implemented in the UCLC ℓ as described in details by [44].

2.2 Angular power spectrum calculation

In full-sky analyses, the APS can be calculated by expanding the projected cosmological fields into spherical harmonics and using Equation 2.7. The partial sky coverage, on the other hand, requires taking into account the coupling of different multipoles as introduced by the geometry of the considered region. We employ the pseudo- C_ℓ formalism as implemented in the NaMaster software [50]. It relates the observed APS, \hat{C}_ℓ , and the true one, C_ℓ , as $\hat{C}_\ell = \sum_{\ell'} M_{\ell\ell'} C_{\ell'}$, where mode-coupling matrix, $M_{\ell\ell'}$, depends only on the geometry of the considered sky area [51]. After analytically calculating this matrix, it is inverted to estimate the C_ℓ .

Here, we measure the pseudo- C_ℓ 's, for auto- and cross-correlation, for 51 linearly spaced multipole bands with width $\Delta\ell = 15$, to guarantee the mode-coupling matrix to be invertible.

3 Synthetic data

In this section, we describe the production of synthetic sky maps for both tracers considered here, namely, the BINGO-like 21 cm IM and the LSST-like photometric galaxy catalogs. We follow closely

the methodology described in [52–54] for the BINGO-like simulations and in [42, 55–57] for the LSST-like simulations. All simulations are produced using HEALPix pixelization scheme [58], with the common resolution of $N_{\text{side}} = 256$.

We use the Full-sky Log-normal Astro-fields Simulation Kit⁷ [FLASK; 59], which generates lognormal realizations of the sky in tomographic redshift bins (z -bins). FLASK uses as input the theoretical auto- and cross-APS, $C_{XY}^{ij}(\ell)$, of the cosmological fields (all possible combinations of different tracers and redshift bins) accounting for their respective projection kernels (selection functions), $\phi(z)$, for the 21 cm IM, and $n(z)$, for the galaxy number count distribution (see section 2.1). These realizations mimic the statistical properties of these matter tracer fields, such as their clustering and log-normal distribution. The theoretical $C_{XY}^{ij}(\ell)$ employed here were calculated using the UCLCℓ code. We follow companion papers [53, 60] and assume our fiducial cosmological model as given by the WMAP 5-year results [61], $\Omega_m = 0.26$, $\Omega_b = 0.044$, $\Omega_\Lambda = 0.74$, and $H_0 = 71 \text{ km s}^{-1} \text{ Mpc}^{-1}$.

In the case of 21 cm IM, our semi-realistic simulations also account for observational and instrumental aspects, such as the sky coverage, instrumental thermal noise and the presence of foreground contaminants, as we describe below.

3.1 H_I intensity mapping simulation

3.1.1 Cosmological signal

A total of 1500 independent realizations of the projected cosmological H_I signal were produced using FLASK. We consider the redshift range $0.127 < z < 0.449$, which corresponds to the frequency interval 980 – 1260 MHz, in which the BINGO radio telescope will operate. This range is divided into 30 uniform frequency bands, each with a bandwidth $\Delta\nu = 9.33 \text{ MHz}$, corresponding to z -bins width of Δz varying from ~ 0.010 to 0.015 for low to high z -bins. The values of $\Omega_{\text{H I}}$ and $b_{\text{H I}}$ in each H_I z -bin ranges from 3.03×10^{-4} to 2.81×10^{-4} and from 1.15 to 1.01, respectively, decreasing with redshift [60]. We chose to use here the same number of channels used in previous BINGO papers [53, 54, 60, 62, 63] and we will identify them with numbers from 1 to 30 with increasing redshift. However, it is worth reminding that BINGO hardware allow other choices for the number of frequency bands. This number will be defined taking into account what is most suitable for cosmological analyses, as well as for the foreground cleaning process [52].

3.1.2 Sky coverage, instrumental effects and foreground signals

BINGO is designed to survey a sky area of 5324 square degrees (sky fraction of $f_{\text{sky}} = 0.129$), in sky transit mode, covering a strip of $\Delta\delta = 14.75^\circ$ wide at declination centered in $\delta = -15^\circ$. To minimize contamination of astrophysical sources from the Galactic plane, we use a mask reproducing the BINGO footprint, including a Galactic cut to remove strong foreground emission [see 52, 53]. This mask is apodized with a 5 deg cosine transition using the NaMaster⁸ code [50], avoiding the impact of sharp edges.

The foreground emissions from Galactic and extragalactic sources are the primary contaminant to the 21 cm intensity mapping signal. The total observed signal combines the foregrounds, the cosmological H_I signal, and instrumental noise [8],

$$T_{\text{obs}}(\nu, \hat{\mathbf{n}}) = T_{\text{H I}}(\nu, \hat{\mathbf{n}}) + T_{\text{foregrounds}}(\nu, \hat{\mathbf{n}}) + T_{\text{noise}}(\nu, \hat{\mathbf{n}}). \quad (3.1)$$

Following [52–54, 63], we employ the *Planck* Sky Model software [PSM; 64] to simulate the contribution of the main foreground components in each of the 30 BINGO frequency bands. Our simulations include the following components:

⁷<http://www.astro.iag.usp.br/flask/>

⁸<https://namaster.readthedocs.io/en/latest/>

- **Galactic Synchrotron Emission:** The dominant foreground component at the BINGO frequencies. The simulation is based on the 408 MHz all-sky map produced by [65], extrapolated to the BINGO frequency range using a spatially variable spectral index map derived from [66]. This model accounts for variations in synchrotron spectral properties across the sky.
- **Galactic Free-Free Emission:** Modeled using the H α emission map from [67]. The emission is scaled uniformly across the sky with a slowly varying spectral dependence, providing a smooth foreground template for subtraction.
- **Thermal Dust Emission:** Simulated using templates derived with the GNILC method applied to Planck 2015 data [15]. Dust spectral index and temperature maps are fitted to GNILC maps in multiple frequencies and extrapolated to the BINGO bands using a modified blackbody law.
- **Anomalous Microwave Emission (AME):** Simulated using a high-resolution thermal dust template derived from Planck observations. The scaling of AME to low frequencies is based on the ratio between AME and thermal dust found in [68]. This component is extrapolated to BINGO frequencies using a single emission law.
- **Extragalactic Point Sources:** Modeled using point source catalogs at 850 MHz and 4.85 GHz [68]. A population of sources below the detection threshold is simulated based on theoretical number counts, ensuring the maps accurately reflect the flux distribution of faint extragalactic sources.
- **Sunyaev-Zeldovich (SZ) Effects:** Modeled using the number density as a function of mass from existing galaxy clusters, while the redshift is predicted following [69].

After including the foreground contaminants, the simulated maps are convolved with the telescope beam, approximated here by a Gaussian function with a full width at half maximum (FWHM) of $\theta_{FWHM} = 40$ arcmin for all frequency bands [see 17, for a complete description of the BINGO beam]. Finally, we add thermal (white) noise, generated as described in [63]. The noise level per pixel is estimated considering a system temperature of 70 K, with 5 years of observation and a set of 28 horns, assuming the arrangement design as planned for Phase 1 of the BINGO telescope observation [17, 62, 70]. From the expected noise level per pixel (the same for all frequencies; see [52, 63] for details), we can produce as many realizations of thermal noise maps as needed.

3.2 Photometric galaxy catalog simulation

We adopt the radial selection function for the LSST photometric galaxy catalog as described in [55], parametrized as:

$$\frac{dN}{dz} \propto z^2 \exp\left[-\left(\frac{z}{z_0}\right)^\beta\right], \quad (3.2)$$

where $z_0 = 0.24$ and $\beta = 0.90$, taken from [56], were derived by fitting to the LSST mock galaxy catalog CATSIM⁹ to reproduce the expected performance over 10 years of observations of LSST in terms of depth, photometric redshift quality, and galaxy number density.

The LSST-like simulations are produced with the FLASK package, taking as input the theoretical auto- and cross-APS, as well as the radial selection function (Eq. 3.2), in order to generate Poisson sampled lognormal realizations of the projected galaxy number counts in each redshift bin. The redshift distribution, $n(z)$, for each tomographic bin is modeled by convolving the radial selection

⁹<https://www.lsst.org/scientists/simulations/catsim>

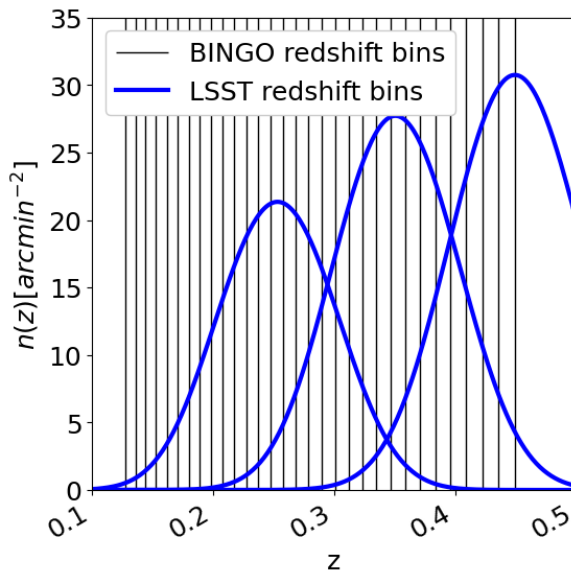


Figure 1: Comparison among BINGO and LSST redshift bins used on the analyses. The black vertical lines delimit the 30 BINGO redshift bins. The blue curves represent the first three LSST photometric redshift bins expected for 10 years of observations (with photo- z error values, σ_z , of 0.0375, 0.0405 and 0.0435) [55], chosen given the overlap with BINGO redshift range.

function with a Gaussian distribution centered at the mean redshift \bar{z} and standard deviation given by the photometric redshift error, $\sigma_z = 0.03(1 + z)$ [55]. Here, we consider only the first three redshift bins from the ten bins expected for 10 years of LSST survey, centered at $\bar{z} = 0.25, 0.35$ and 0.45 (blue curves in Figure 1). The photometric redshift errors on each tomographic bin are, respectively, $\sigma_z = 0.0375, 0.0405$ and 0.0435 , and the galaxy bias $b_G = 1.13, 1.19, 1.25$.

4 H_I signal detection

In this section, we describe the methods employed to recover the 21 cm cosmological signal from the contaminated maps, presenting the foreground cleaning process and the estimated APS. The statistical significance of the auto- and cross-correlation detection are also evaluated.

4.1 Foreground cleaning

Recovering the cosmological signal in 21 cm IM experiments requires an efficient foreground mitigation strategy, since contamination by astrophysical sources can exceed the cosmological signal by several orders of magnitude. To address this challenge, we use the Generalized Needlet Internal Linear Combination (GNILC) method [71], which rely on the characteristic smooth spectral dependence of these contaminants in contrast to the cosmological signal [8, 14]. GNILC is a nonparametric component separation technique that uses spatial and spectral information to separate foregrounds from the signal of interest. In particular, the method relies on the expected high correlation of the Galactic and extragalactic emissions among the frequency bands, in contrast to a weak correlation of the 21 cm signal between different bands. As the thermal noise has no such correlation, GNILC recovers the cosmological H_I IM along with the thermal noise component in each frequency band. This foreground cleaning method has already been tested on synthetic 21 cm IM data [15], showing

good performance in the case of future BINGO observations [52, 62, 63]. Here, we use the GNILC method following the procedure of [52] for the BINGO case.

As discussed in [52], a byproduct of the GNILC algorithm are the ILC filters constructed for each needlet (a kind of bandpass filter in harmonic space, defined here by the index k), input required by the method, and for each pixel of the maps produced by them, in such a way as to the foreground contaminants, while preserving the 21 cm signal and the thermal noise. Each ILC filter, $\mathbf{W}^{(k)}(p)$, is applied to a synthetic observation (cosmological signal and contaminants), $\mathbf{x}^{(k)}(p) = \mathbf{s}^{(k)}(p) + \mathbf{n}^{(k)}(p) + \mathbf{f}^{(k)}(p)$, where $\mathbf{s}^{(k)}(p)$, $\mathbf{n}^{(k)}(p)$, and $\mathbf{f}^{(k)}(p)$ are the 21 cm signal, thermal noise, and foreground contamination, respectively, at each pixel p and at each needlet scale (k). The set of filtered maps, $\hat{\mathbf{s}}^{(k)}(p) = \mathbf{W}^{(k)}(p)\mathbf{x}^{(k)}(p)$, for each needlet angular scale k , are combined to obtain the reconstructed 21 cm signal plus noise map at each frequency band. Omitting the indices p and k , the reconstructed maps $\hat{\mathbf{s}}$ can be written as

$$\hat{\mathbf{s}} = \mathbf{W}\mathbf{s} + \mathbf{W}\mathbf{n} + \mathbf{W}\mathbf{f}, \quad (4.1)$$

where the ILC filter \mathbf{W} can be used to quantify the impact of each component, such that $\mathbf{W}\mathbf{n}$ accounts for thermal noise, and $\mathbf{W}\mathbf{f}$ corresponds to the residual foreground contamination. Besides the residual contamination, it is also expected that, due to the product $\mathbf{W}\mathbf{s}$, a fraction of the cosmological signal \mathbf{s} is lost during the foreground cleaning process (see, for example, [25, 26]), which affect the cross-correlation with galaxy surveys, as we discuss in the next sections.

APS debiasing process: To recover the APS from the 21 cm signal and its correlation with a galaxy sample, we implement a debiasing procedure, in the same fashion as [52, 63]. For auto-correlation, this procedure accounts for two steps: subtracting the expected average contribution of the thermal noise, $\hat{C}_\ell^{\text{noise-ILC}(i)}$ (additive bias), and dividing by a scale-dependent factor, $\hat{S}^i(\ell)$ (multiplicative bias), to account for a suppression of the APS due to the loss of the 21 cm signal.

In our case, the estimation of the additive bias is done by passing 50 noise realizations, for each frequency band, through the ILC filters produced as described previously. We then average the APS of the 50 ILC-reconstructed noise maps to obtain the $\hat{C}_\ell^{\text{noise-ILC},i}$. It is important to mention that these 50 noise realizations are different from the noise realizations used to obtain the synthetic observation maps.

To obtain $\hat{S}^i(\ell)$, the multiplicative bias for each redshift bin (frequency band), we apply the ILC filter to 50 realizations of 21 cm simulated maps, and then average the ratio between the APS from the ILC filtered 21 cm maps, $C_\ell^{\text{Hi-ILC}(i)}$, and from the input ones, $C_\ell^{\text{Hi}(i)}$, that is, $\hat{S}^i(\ell) = \langle C_\ell^{\text{Hi-ILC}(i)} / C_\ell^{\text{Hi}(i)} \rangle$. The corrected (debaised) APS for the m th 21 cm IM realization at z -bin i is given by,

$$\tilde{C}_\ell^{\text{GNILC-deb}(i)}|_m = \frac{\hat{C}_\ell^{\text{GNILC}(i)} - \hat{C}_\ell^{\text{noise-ILC}(i)}}{\hat{S}^i(\ell)} \Big|_m. \quad (4.2)$$

This correction procedure, originally designed for autocorrelation analyses, is extended here to cross-correlation by setting the additive term to zero, since the white noise contaminating the cosmological signal is not correlated with galaxy maps. The multiplicative bias is employed to account for the suppression of the cross-APS due to the 21 cm signal lost during foreground removal:

$$\tilde{C}_\ell^{\text{GNILC-deb}(i),\text{gal}(j)}|_m = \frac{\hat{C}_\ell^{\text{GNILC}(i),\text{gal}(j)}}{\hat{S}^{i,j}(\ell)} \Big|_m. \quad (4.3)$$

$\hat{S}^{i,j}(\ell) = \langle C_\ell^{\text{Hi-ILC}(i),\text{gal}(j)} / C_\ell^{\text{Hi}(i),\text{gal}(j)} \rangle$ is obtained averaging the ratio between the cross-APS among the filtered \mathbf{s}' map and the corresponding galaxy density realization, $C_\ell^{\text{Hi-ILC}(i),\text{gal}(j)}$, and among the

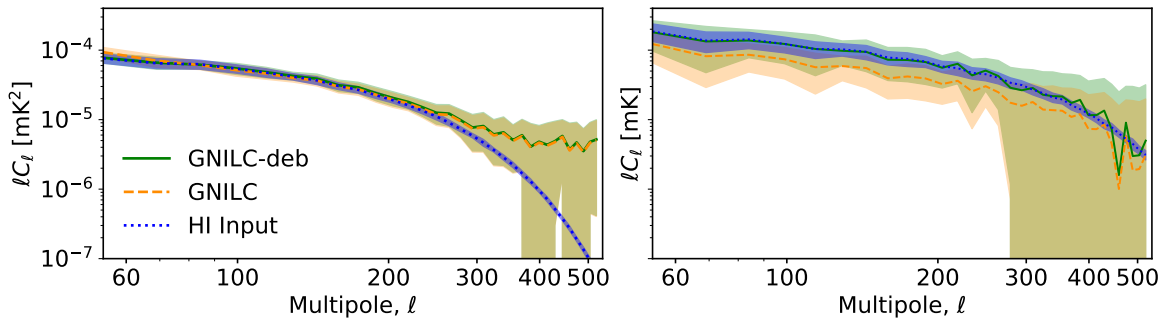


Figure 2: Comparison among the mean APS and 68% regions from 50 realizations before (GNILC; green solid lines) and after (GNILC-deb; orange dashed lines) applying the debiasing process (see text for details). Results from the input HI maps are shown in blue (HI Input; blue dot lines). Left and right panels correspond to auto-APS of BINGO z -bin 14 ($\bar{z}_{HI} \approx 0.252$) and its cross-APS with the first LSST photo- z bin ($\bar{z}_G \approx 0.250$), respectively.

original \mathbf{s} map and the same galaxy density map, $C_\ell^{\text{HI}(i),\text{gal}(j)}$. Again, the average is obtained using 50 pairs of 21 cm IM and galaxy density maps. Figure 2 presents a comparison of the APS for the two cases.

Since the foreground cleaning process is computationally demanding, we apply the GNILC method to 50 ($m = 1, 2, \dots, 50$) synthetic observations, employing the debiasing process for each resulting auto- and cross-APS. Notice that, for each m map, the multiplicative bias is estimated using a different set of 50 HI IM realizations, not used as the cosmological signal in the synthetic observations.

In addition to the 50 cleaned BINGO-like maps, we follow [53, 54] and produce a set of 1500 realizations, mimicking these GNILC outputs (intended to be used to construct the covariance matrix employed in Section 5). For this, we simply add a different realization of the white noise component to each of the 1500 HI IM realizations, including the expected residual foreground contribution estimated using the ILC filter, \mathbf{Wf} (see Equation 4.1). Since we run GNILC 50 times (each m map), we use the 50 resulting estimates of the residual foreground contribution to contaminate the 1500 realizations.

While the white noise is different from one realization to another, the foreground residual is repeated every 50 realizations. This way we can produce a larger set of fast BINGO-like simulations, while avoiding to perform the computationally expensive foreground cleaning process for each of them. For this set of simulations we do not need the repetition of the two steps debiasing process of the (auto- and cross-) APS, since no cosmological signal is lost. For autocorrelation, we perform a simpler debiasing by subtracting the expected constant noise amplitude, N_ℓ (the theoretical noise level); cross-APS does not require any debiasing in this case.

4.2 Results

In this section, we present the results for estimating auto- (HI-HI) and cross- (HI-galaxies) APS in section 4.2.1. The impact of thermal noise and foreground residual contamination is individually evaluated. The role of photometric uncertainties in the cross-APS calculations is also quantified. The statistical significance of a potential detection of both auto- and cross-APS signals based on the simulations will be quantified in Section 4.2.2.

BINGO	\bar{z}_{HI}	LSST	\bar{z}_G
Hr 14	0.252	G1	0.250
Hr 23	0.353	G2	0.350
Hr 30	0.442	G3	0.450

Table 1: Summary of the photometric z -bins and the respective H_I IM z -bins centered on them. Numbering the BINGO z -bins from 1 to 30, the first and second columns list the number of the three chosen bins and their mean redshift value. The same information is listed for LSST at third and fourth columns, numbering their z -bins from 1 to 3.

4.2.1 Angular power spectrum estimation

To assess the impact of individual contaminants on the 21 cm signal, we analyze the angular power spectra of H_I maps under four different scenarios:

- (i) input (original) H_I maps (“HI Input”, blue curve in Figure 3),
- (ii) H_I maps contaminated with white noise, with the subsequent subtraction of the expected noise amplitude N_ℓ from the auto-APS, that is, H_I signal contaminated by a residual contribution of white noise (“HI + WN”, cyan curve in Figure 3),
- (iii) BINGO-like simulations, adding the white noise and foreground residuals to the H_I signal, with the subsequent subtraction of the estimated noise amplitude N_ℓ from the auto-APS (“HI + WN + Fg”, purple curve in Figure 3), and
- (iv) H_I signal reconstructed using the GNILC cleaning method, with the application of additive (for auto-APS) and multiplicative (for auto- and cross-APS) debiasing corrections (“GNILC-deb”, green curve in Figure 3).

All of these scenarios account for the instrumental beam effect. We estimate the cross-correlation among the three z -bins of LSST-like galaxy density samples and 30 BINGO-like H_I IM realizations (3×30 cross-APS) for each of these four scenarios, as well as the autocorrelation for all H_I IM z -bins. Unless stated otherwise, we will show, as illustrative examples throughout this section, the results obtained using the three BINGO z -bins closest to the center of the LSST redshift distributions (see Fig. 1), as summarized in Tab. 1. As we show later, these are the cases that produce a higher signal-to-noise ratio for the cross-correlation case.

Figure 3 shows the mean and 68% region (the 1σ dispersion of the 50 APS curves) of the APS from 50 realizations, for each of the four scenarios listed above. The top panel shows an example of auto-APS for one of the BINGO z -bins, from where we observe significantly larger 68% regions due to the presence of contaminants, in particular at high multipoles (small scales), where the thermal noise amplitude becomes larger than the cosmological signal. White noise (HI + WN case) seems to be the main responsible for this behavior, given that the inclusion of foreground residual (HI + WN + Fg case) and the implementation of the component separation process (GNILC-deb case) results in 68% regions similar to the HI + WN case. The remaining panels of Figure 3 display the results for the cross-APS between three BINGO z -bins and each of the LSST z -bins (as listed in Tab. 1).

We also observe a clear power excess in the mean curves of the auto-APS spectra, compared to the HI Input scenario. The excess appears in the higher multipoles of the auto-APS, introduced by the contaminants, which is not observed in the cross-APS. These results also show that, even though the residual contamination by white noise and foregrounds do not correlate with the galaxy distribution,

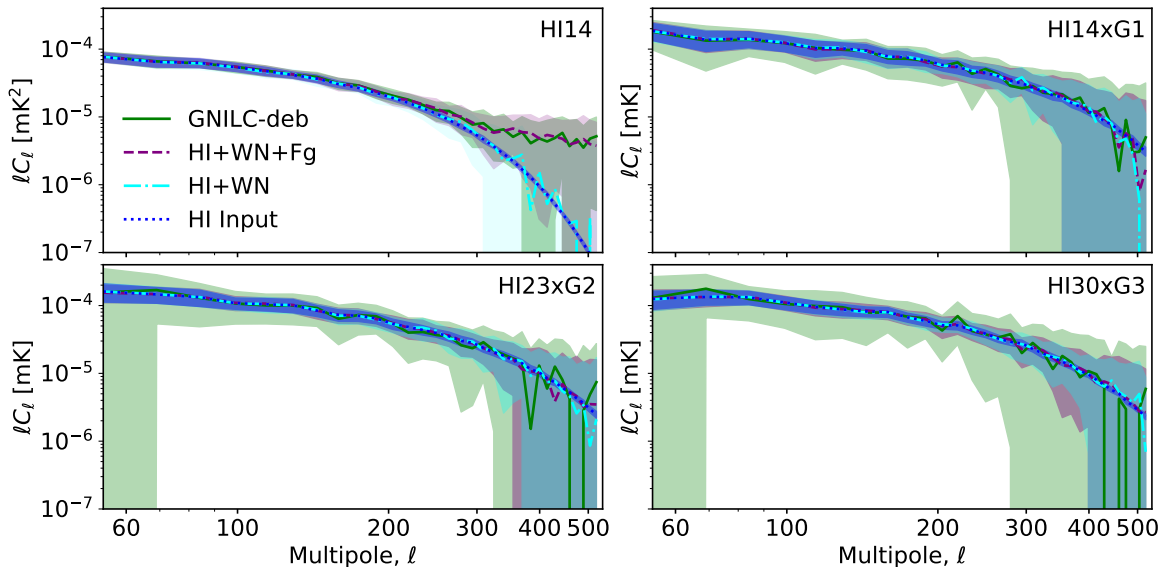


Figure 3: Comparison of the mean APS and 68% regions from 50 realizations for four different scenarios. Colors and scenarios are discussed in the beginning of section 4.2.1. Upper left panel shows the auto-APS for BINGO z -bin number 14. The other three panels show the cross-APS among BINGO and LSST bins as indicated in the top right corner of each panel (see definitions in Table 1).

not contributing to the amplitude of the APS, they boost the noise in cross-correlation, increasing the 68% region, as expected.

Similarly to the auto-APS case, white noise seem to be the main driver of the increase of the 68% region for cross-APS. In addition, one can see that the component separation process also impacts the estimate of the cross-APS, contributing with an additional increase of the 68% region, likely due to the loss of H α signal. Comparing the first and second panels of Fig. 3 (for the same H α IM z -bin), we also notice a wider 68% region for the cross-APS compared to auto-APS, even when comparing only results from the H α Input scenario. We believe this effect is associated to the photometric redshift error, and will be discussed later in this section.

Before investigating the impact of photo- z errors, we evaluate the SNR of auto and cross-APS, presented in Figure 4. Comparing blue and green curves, we can see, on both the auto- and cross-APS, the impact of foreground residuals and thermal noise remaining in the H α IM maps after the component separation and debiasing processes, in particular for higher multipoles ($\ell \gtrsim 300$). These results also indicate that the cross-APS is more impacted by cleaning process and residual contamination, with a decrease in the SNR over the entire multipole range, while the auto-APS does not show significant decrease for $\ell \lesssim 100$. In both cases, the SNR becomes smaller than 1 for $\ell \gtrsim 300$, except in the case of the auto-APS from the last redshift bin (last panel of Fig. 4).

It is worth noticing from Fig. 3 that the amplitude of the auto-APS of the H α IM z -bin number 14 (first panel) is lower than that from its cross-correlation with the first z -bin of the galaxy distribution (second panel). Still, the first panel of Fig. 4 shows the SNR to be higher for its autocorrelation, even for the H α Input scenario. This behavior is a consequence of the larger 68% region for cross-correlation, showing its impact on the cross-correlation detection in the future BINGO and LSST surveys. As we mentioned before, this larger dispersion might be associated with the photometric redshift uncertainty, σ_z , a suspicion we explore through the null test described below.

H α IM instruments survey the Universe using a tomographic approach, where each volume

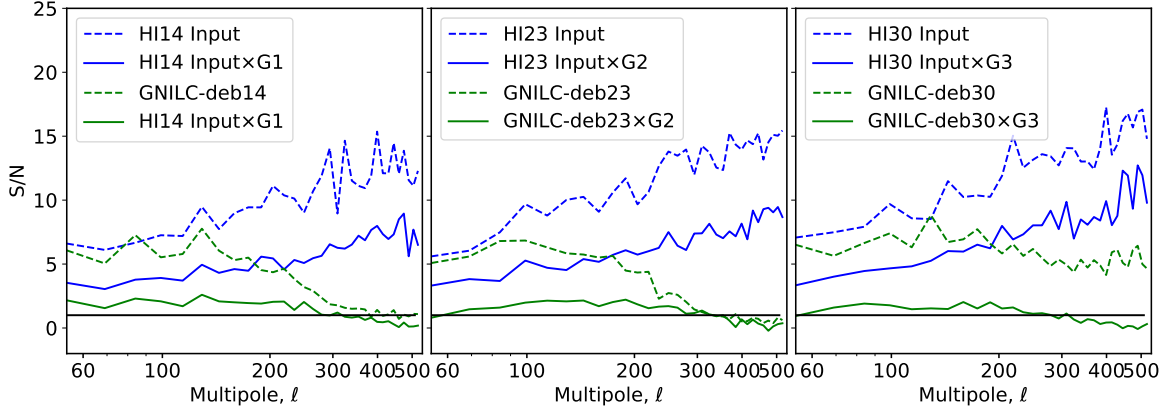


Figure 4: Signal-to-noise ratio (SNR) for H I IM auto-APS (dashed lines) and their cross-APS with the galaxy density maps (solid lines), averaged over 50 realizations. Blue and green lines show results from scenarios H I Input and GNILC-deb, respectively. BINGO and LSST z-bins are indicated in each panel (see definitions in Table 1). Black horizontal line represents $\text{SNR} = 1$.

"slice" corresponds to very narrow frequency bands, consequently to a high radial resolution. Current galaxy photometric surveys use filters that, by construction, covers a much larger redshift interval with consequent poorer redshift resolution, as shown in Figure 1. The poor photo- z accuracy can lead to galaxies being assigned to a bin in which they are not physically present. In this work, we computed cross-correlations of BINGO-like H I maps with each of the three LSST z -bins using their entire photometric galaxy distribution, instead of slicing them into 30 narrow z -bins with widths matching the BINGO bins, as described in [39]. Contrary to their results, we did not find a degradation in power of the cross-APS (see Fig. 3).

As a safety check, we implement a null test to investigate the impact of the presence of galaxies in the photo- z bin that do not contribute to the H I signal with which it is being cross-correlated (non-correlated galaxies). We estimate the cross-correlation between a fixed H I IM realization and 500 maps generated as Gaussian random distributions with zero mean and standard deviation σ . Given that there is no spatial correlation among them, the full Gaussian distribution mimics the presence of non-correlated galaxies. We repeat this procedure for four different values of σ , namely 0.0110, 0.0375, 0.0405, and 0.0435, each of them representing the width (error) of the redshift bin. Notice that the former σ value matches the width of a H I IM z -bin, while the other three values match the photometric redshift uncertainty, as described in Secs. 3.1.1 and 3.2).

Figure 5 show the average (expected to be close to zero) and 68% error bars over the 500 cross-correlation estimates, for each σ . As we can see, although the σ value of the Gaussian random distributions does not introduce any bias in amplitude, it impacts the statistical uncertainty on the APS estimates, leading to larger 68% error bars the larger the σ value, affecting the entire range of multipoles. This noise-like behavior explains why the autocorrelation presents higher SNR compared to cross-correlation (Fig. 4), even with the fact that optical galaxy data and H I IM contaminants are uncorrelated. Therefore, cross-correlating H I IM with the entire photometric galaxy distribution preserves the cross-APS amplitude, while introducing a higher uncertainty in the estimated signal (given by the large 68% regions). Moreover, the null test confirms that the presence of thermal noise in the H I IM maps increases significantly the 68% regions at high multipoles, where it starts to dominate the cosmological signal, although not affecting the amplitude of the cross-APS (see Fig. 3).

Finally, we evaluate the impact of each contaminant (white noise and foreground residuals), as

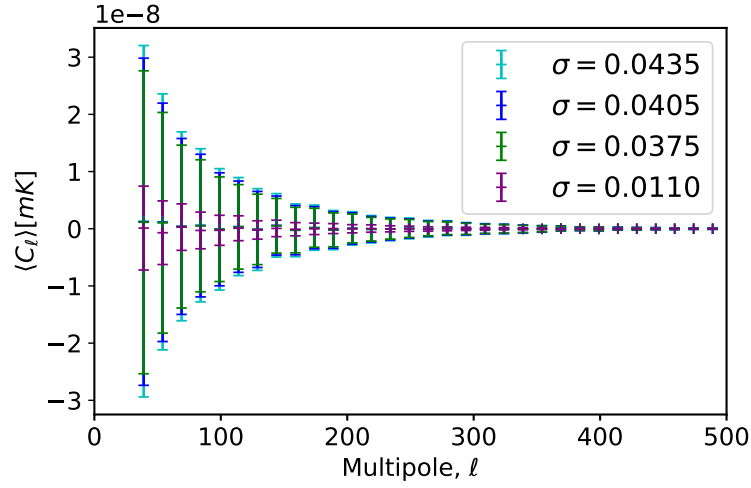


Figure 5: Null test: Average and 68% error bars from the cross-correlation among a synthetic HI IM map and 500 (non-correlated) maps generated as Gaussian random distributions with zero mean and standard deviation of σ . The results are shown for four values of σ , representing the width of the photometric redshift distribution of the galaxies (cyan, blue, and green) and the HI IM z -bin (red).

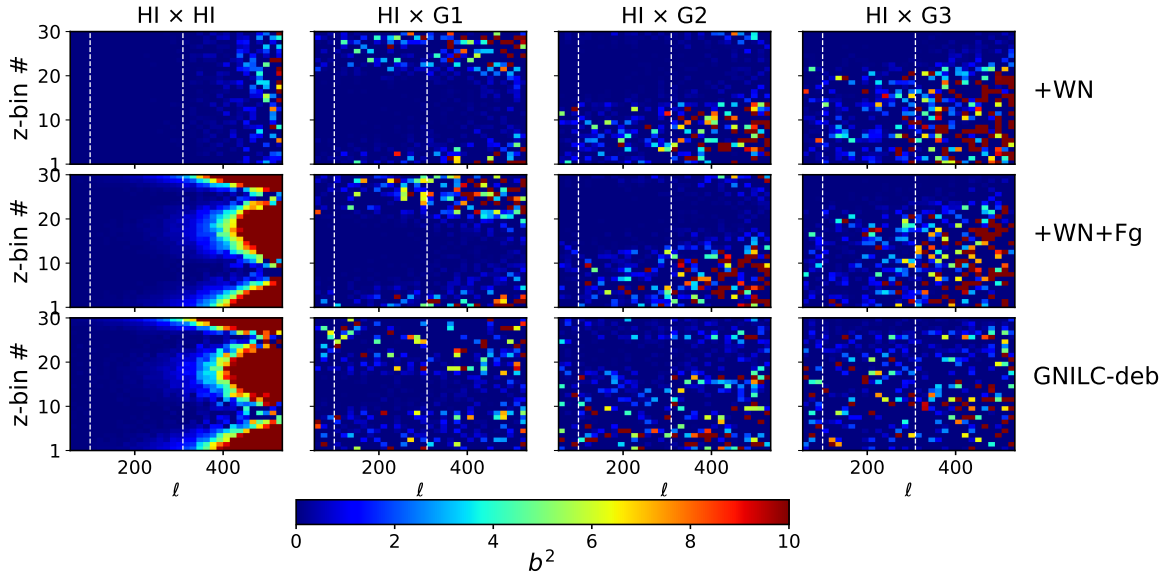


Figure 6: Impact of the white noise, foreground residues, and component separation process on the auto- and cross-APS. The panels show the relative difference between the contaminated and clean angular power spectra (Eq. 4.4) for the 30 BINGO redshift bins (y-axes). Top row corresponds to contamination by white noise (HI+WN), middle row describes contamination by white noise and foreground residues (HI+WN+Fg), and bottom row is the GNILC-deb result. Columns show auto-correlation (first column) and cross-correlation with the three LSST photometric bins (other three columns). White dashed lines in $\ell = 99$ and $\ell = 309$ indicates the range in multipoles considered in the parameter estimations (see Section 5).

well as the component separation process, on the auto- and cross-APS for all BINGO bins in each scenario (ii–iv). For this, we use the relative difference between them and the APS from the H_I Input scenario, $C_\ell^{\text{H}_I \text{ Input}}$, defined as

$$b^2(\ell) = \left\langle \frac{C_\ell}{C_\ell^{\text{H}_I \text{ Input}}} - 1 \right\rangle, \quad (4.4)$$

as a function of multipole, ℓ , and averaged over the 50 realizations. Figure 6 shows the b^2 factor for the auto-APS from all 30 BINGO redshift bins, as well as their cross-APS with each of the three LSST photometric redshift bins. The first column shows how the white noise impacts the auto-APS at high multipoles and how the contribution of foreground residuals significantly increases the discrepancy with respect to the original H_I Input signal around $\ell \gtrsim 300$. The impact varies with the redshift bin, showing a worse recovery of the H_I signal for frequency bands closer to the border of the BINGO frequency range. As shown by [52], using a larger number of frequency bands can improve the performance of the GNILC, around the center and borders (see bottom right panel of their Fig. 8).

The cross-correlation plots in Fig. 6 show a better estimate of the cross-APS for H_I signal z -bins closer to the center of the photometric galaxy distribution. Moving away from the center causes the cross-correlation signal to weaken and become increasingly dominated by contaminants. Compared to the impact of white noise (H_I + WN; first row), the addition of foreground residuals further restricts the cross-correlation signal to the center of the galaxy distribution, with a more severe restriction when properly using the component separation process to recover the H_I signal.

Figure 7 presents the b^2 amplitude as a function of the multipole for the auto- and cross-APS of the BINGO z -bins number 14, 23, and 30, the closest to the center of the LSST galaxy distribution (Tab. 1). This figure highlights how the auto-APS are significantly affected by residual contamination at multipoles $\ell \gtrsim 250 - 270$ (a scale-dependent distortion), with a more pronounced effect from the last redshift bin (the border effect associated with the GNILC method as mentioned previously). On the other hand, the cross-APS amplitudes are considerably less affected by the residual contamination, exhibiting an approximately scale-independent b^2 factor. This enforces the power of the cross-correlation analyses; unlike the autocorrelation, where contamination dominates from relatively low multipoles, the cross-spectra, using H_I IM z -bins closest to the center of the photometric galaxy distribution, are much less affected at higher multipoles. A similar result is observed by [38], where the authors also found a scale dependence of the b^2 factor with multipole for autocorrelation, and mild ℓ -dependence for the cross-correlation.

4.2.2 Statistical Significance

To quantify the statistical significance with which the APS would be detected, we compute $\sqrt{\Delta\chi^2} = \sqrt{\chi^2 - \chi_{\text{null}}^2}$, the difference between the χ^2 value calculated for a given simulation using our model (Sec. 2.1), and using a null model with zero (auto- or cross-) APS. For each scenario, the $\sqrt{\Delta\chi^2}$ value is estimated for 50 realizations, but using all the 1500 realizations to obtain the covariance matrix. For the GNILC-deb realizations, we use the covariance matrix calculated from the 1500 fast simulations (H_I + WN + Fg). In all cases, we employ the multipole range $99 < \ell < 309$ (vertical dashed white lines in Fig. 6), chosen to avoid multipole with poor SNR and to maximize the statistical significance. Figure 8 shows the average and 68% error bars from the $\sqrt{\Delta\chi^2}$ estimated for the autocorrelation of each of the 30 BINGO z -bins and their cross-correlation with the three LSST photometric redshift bins, for the scenarios (i) to (iv) listed in Section 4.2.1.

The statistical significance for the autocorrelation of each BINGO z -bin is shown in the first panel of Fig. 8, showing a larger value of $\sqrt{\Delta\chi^2}$ the higher the redshift. This result also shows that the detectability of the H_I signal at high redshifts is impacted by the inclusion of contaminants ($z \gtrsim 0.25$).

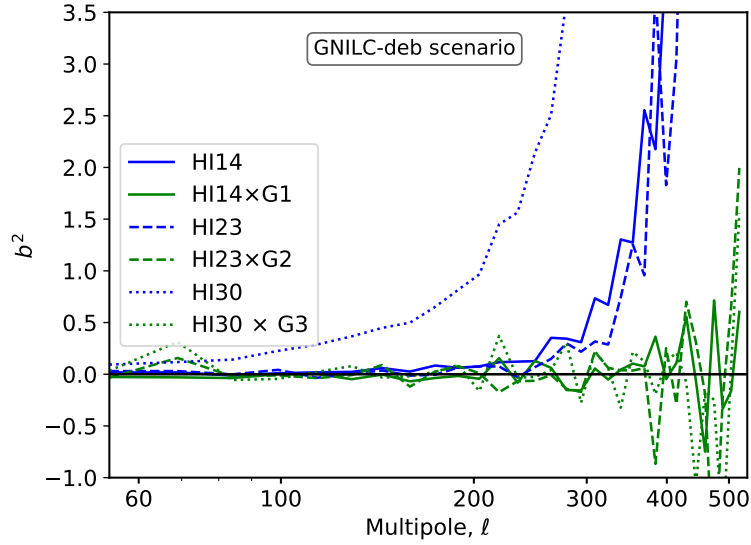


Figure 7: b^2 factor for HI auto-APS (blue curves) and cross-APS (green curves) for GNILC-deb scenario. The solid, dashed, and dotted lines represent results using the BINGO bins described in Table 1.

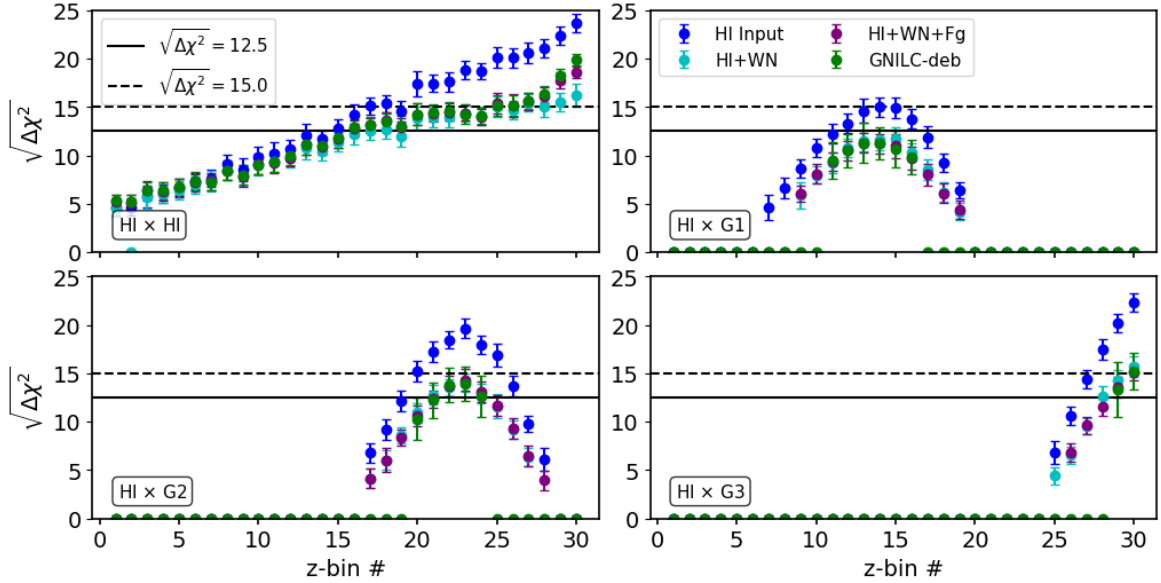


Figure 8: Statistical significance of the HI signal detection through the autocorrelation of the 30 BINGO z -bins and their cross-correlation with each of the 3 LSST photo- z bins (see Figure 1). Upper left panel: auto-APS for the 30 BINGO z -bins. Upper right: cross-APS among all BINGO z -bins and LSST bin 1 ($\bar{z}_G \approx 0.25$). Lower left: cross-APS among all BINGO z -bins and LSST bin 2 ($\bar{z}_G \approx 0.35$). Lower right: cross-APS among all BINGO z -bins and LSST bin 3 ($\bar{z}_G \approx 0.45$). In all the cases, $\sqrt{\Delta\chi^2}$ is calculated employing the multipole range $99 < \ell < 309$. The solid and dashed horizontal lines denote $\sqrt{\Delta\chi^2} = 12.5$ and 15.0 , respectively, for reference.

The similar statistical significance among the three scenarios with contaminants (ii-iv) indicates the thermal noise, present in all of them, as the main responsible for such degradation. Notice that, within the BINGO redshift range, higher redshifts are more affected by white noise because it starts to dominate the cosmological signal at smaller multipoles compared to lower redshifts, as discussed by [53].

The remaining panels of Fig. 8 show the statistical significance derived from the cross-correlation between of the 30 BINGO bins and each of the three LSST bins (cf. Figure 1). For each LSST bin, the peak of the significance occurs at the center of the galaxy photo- z bins, where the number of galaxies contributing to both tracers is maximized and the cross-APS is more accurately estimated (see Section 4.2.1 and Fig. 6). Again, the three three scenarios with contaminants (ii-iv, the cyan, purple, and green dots) show similar statistical significance, indicating that the impact of foregrounds is negligible compared to the thermal noise, even with the application of additive debiasing correction. Despite the GNILC-deb maps (green dots) and the fast simulations (purple dots) yielding similar significance values around the center of the LSST photo- z bins, the former is more restricted to center of the galaxy distribution, with some of the green dots further away of the center dropping to a significance close to zero. This suggests that our fast simulations are not representative enough of the foreground cleaned maps, indicating that the degradation of the H I signal by the component separation process impacts the cross-correlation when using H I redshift bins away from the center of the galaxy distribution.

Comparing the results shown in Fig. 8 from auto- and cross-APS for H I z -bins closer to the center of the photo- z galaxy distributions, we find very similar statistical significance among them. This indicates that, although the cross-correlation signal, on average, is not degraded in amplitude due to the poor photometric redshift determination. Differently from the results presented by [39], the noise-like effect introduced by the presence of galaxies not contributing to the H I z -bin, as well as the presence of residual contamination in the H I maps, results in a significant deterioration of the statistical significance of their detection. This deterioration is sufficient to make the detection of the cross-correlation signal as likely as the autocorrelation, even with the great advantage of the systematics being uncorrelated to the cosmological signal.

However, it is important to remember that, as a first analysis addressing the use of the full photometric galaxy distribution for cross-correlation with H I IM, our work employ semi-realistic simulations of the future BINGO observations. As such, they lack to account for instrumental effects relevant for intensity mapping experiments, such as the low frequency ($1/f$) noise [18] and the leakage of polarized foregrounds into the intensity data [14, 72]. Additional sources of contamination will certainly impact the H I autocorrelation signal more, but should have a weaker impact in the cross-correlation signal. Additionally, increasing the number of frequency bands should improve the foreground cleaning process [52], providing better auto- and cross-APS estimates, particularly at higher redshifts. This would likely allow improving the statistical significance for the cross-correlation detection using H I z -bins further away from the center of the galaxy distributions.

5 Parameter estimation

As demonstrated by several authors, the cross-correlation of H I IM observations with galaxy catalogs can provide an estimate of the cosmological H I signal [24–27, 45, 73–77]. In this section, we assess the potential of combining simulations of BINGO and LSST data to estimate the product of the degenerate parameters $b_{\text{H}\text{I}}$, $\Omega_{\text{H}\text{I}}$, and the cross-correlation coefficient, r , that characterize the 21 cm signal.

The aforementioned papers, as well as other works in the literature reporting constraints on $b_{\text{Hi}} \Omega_{\text{Hi}} r$, model the matter clustering through the power spectrum in Fourier space. In this work, we show that the APS is a promising alternative to be used in the same task. Following [26], we assume b_{Hi} and Ω_{Hi} to be approximately constant inside the redshift bins, given the narrow width of the z -bin; simulations are generated based on this assumption. In this way, one can move this quantity outside the integrals in Eq. 2.7, such that we have, respectively, for autocorrelation and cross-correlation,

$$C_{\text{Hi}, \ell}^{ij} = (\Omega_{\text{Hi}} b_{\text{Hi}})^2 C_{\text{m}, \ell}^{ij} \quad (5.1)$$

$$C_{\text{Hi}, g, \ell}^{ij} = \Omega_{\text{Hi}} b_{\text{Hi}} r_{\ell} C_{\times\text{g}, \ell}^{ij}, \quad (5.2)$$

where the degenerate quantity, $b_{\text{Hi}} \Omega_{\text{Hi}} r$, is assumed to be scale independent, affecting only the amplitude of the cross-APS model. It is worth noting that the correlation coefficient r that accounts for the stochasticity between the two cosmological fields should be scale dependent [24–26, 45]. However, since it approaches unity on large scales, the scale independency is a reasonable assumption on the scales considered here, $r_{\ell} = r$. In this case, $b_{\text{Hi}} \Omega_{\text{Hi}} r$ and $b_{\text{Hi}} \Omega_{\text{Hi}}$ can be estimated by fitting, respectively, the amplitude of the auto-APS ($C_{\text{Hi}, \ell}^{ij}$) and cross-APS ($C_{\text{Hi}, g, \ell}^{ij}$) and obtained from the simulations.

For autocorrelation, the model $C_{\text{m}, \ell}^{ij}$ corresponds to the matter APS, calculated using the UCLCℓ code and imposing $b_{\text{Hi}} = \Omega_{\text{Hi}} = 1$. For cross-correlation, the model $C_{\times\text{g}, \ell}^{ij}$ corresponds to the cross-APS and already accounts for the galaxy bias b_G and the redshift distribution $n(z)$, both considered as known, given that they can be obtained from galaxy surveys (see, e.g., [55]), again imposing $b_{\text{Hi}} = \Omega_{\text{Hi}} = 1$.

We constrain the degenerate quantities, $b_{\text{Hi}} \Omega_{\text{Hi}} r$ and $b_{\text{Hi}} \Omega_{\text{Hi}}$, through a least-square fit to the amplitude of the auto- and cross-APS obtained from the simulations, similarly to what is done by [26]. We minimize¹⁰ the χ^2 defined as

$$\chi^2(\lambda) = \sum_{k,m} [X_k^i - \lambda x_k^i] [C_{km}^{ij}]^{-1} [X_m^j - \lambda x_m^j], \quad (5.3)$$

where λ is the degenerate quantity to be estimated, i, j refers to the redshift bins, and k, m indices run over the different multipole bands, ℓ . Following our findings from last section, the fitting is performed using the multipole interval $99 \lesssim \ell \lesssim 309$, which is the less affected by residual contamination (best SNR). The terms X_k^i and x_k^i correspond to the measured APS, $C_{\text{Hi}, \ell}^{ij}$ or $C_{\text{Hi}, g, \ell}^{ij}$ and model, $C_{\text{m}, \ell}^{ij}$ or $C_{\times\text{g}, \ell}^{ij}$, respectively; $[C_{km}^{ij}]^{-1}$, corresponds to the rescaled precision matrix¹¹.

Figure 9 compares the estimated values of the degenerate quantities, from fitting both auto- and cross-APS amplitudes, for 50 realizations from each of the four scenarios. For the cross-correlation, we show only the results obtained for the BINGO z -bins closest to the center of the LSST galaxy distribution, that is, for those cross-APS leading to statistical significance higher than unity in Fig. 8.

The results of the present analysis suggest that the application of cross-correlation using our current semi-realistic simulations, the GNILC-deb realizations, introduces no observable systematic error in the average $b_{\text{Hi}} \Omega_{\text{Hi}} r$ values when benchmarked against the Hi input scenario. In contrast, the autocorrelation analyses indicates a displacement in the average $b_{\text{Hi}} \Omega_{\text{Hi}}$ toward larger values at the higher redshifts, a deviation plausibly caused by enhanced the amplitude of the foreground residuals within the corresponding redshift intervals.

¹⁰Implemented using the `curve_fit` function from SciPy [78].

¹¹To mitigate bias in the inverse covariance matrix due to statistical noise, we adopt a rescaled precision matrix as proposed in [79]. Given the number of simulations, N , and the number of entries of the APS data vectors, N_p , the rescaled precision matrix is obtained by $[C_{ij}^{km}]^{-1} \rightarrow (N - N_p - 2)/(N - 1) [C_{ij}^{km}]^{-1}$.

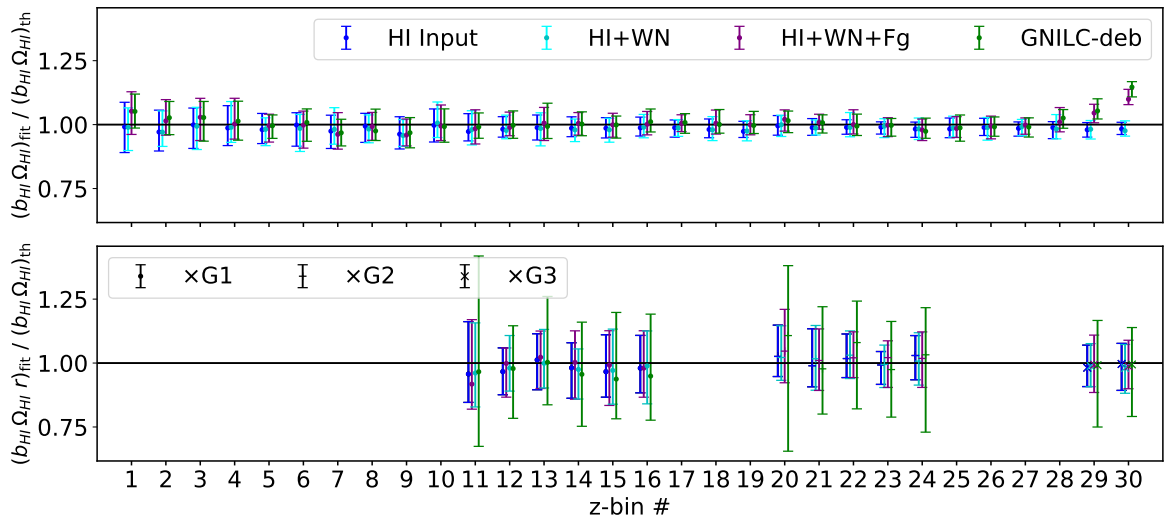


Figure 9: Median and 16 and 84 percentiles (1σ dispersion) of the $b_{\text{HI}} \Omega_{\text{HI}}$ and $b_{\text{HI}} \Omega_{\text{HI}} r$ quantities constrained, respectively, from auto-APS (top panel) and cross-APS (bottom panel) measured from simulations of scenarios (i) to (vi). The x-axis represents the BINGO redshift bin, and the y-axis shows the ratio between the estimated and theoretical values. The bottom panel shows only the results from cross-APS whose statistical significance is higher than unity (green dots in Figure 8). Results from the cross-correlation with the first, second, and third LSST bins are represented by \bullet , $+$, and \times symbols, respectively. Results are slightly shifted to right for better visualization.

Still in Fig. 9, we see that, although the cross-correlation results do not show any shift, it leads to a larger 1σ dispersion of the estimated values compared to the autocorrelation results. Considering the HI Input scenario (blue bars), the cross-correlation with the first, second, and third photo- z bins lead, respectively, to 1σ dispersion at least 2.07, 2.15 and 2.58 times larger than those from the autocorrelation of the corresponding BINGO z -bins. For the GNILC-deb scenario (green bars), the 1σ dispersion from cross-correlation increases by 2.83, 3.44 and 3.69, respectively, with respect to autocorrelation. Such findings from the GNILC-deb case show the combined effect of the photo- z error and the deterioration of the HI signal by the component separation process. Additionally, we show that HI +WN, HI +WN+Fg and GNILC-deb scenarios do not seem to impact significantly the HI Input fitting results for autocorrelation.

Finally, the GNILC-deb scenario leads to 1σ dispersion from 1.16 to 3.65 times larger than those from HI +WN+Fg for cross-correlation. For the BINGO z -bins closest to the center of LSST distributions (see Tab. 1), the 1σ uncertainty in the degenerate quantities, estimated from the GNILC-deb APS, correspond to a fraction of 0.05 and 0.20, respectively, of the theoretical $b_{\text{HI}} \Omega_{\text{HI}}$ and $b_{\text{HI}} \Omega_{\text{HI}} r$ values, from auto and cross-correlation. Since in all the cases the 1σ intervals (68% of the simulations) are far from zero, as can be seen in Fig. 9, our results suggest that it would be possible to detect the HI signal and constrain the degenerate parameters, considering the semi-realistic simulations employed here. Nevertheless, we state that our conclusions might be challenged by real HI data or more complete simulations, conditions under which we expect the autocorrelation results to be more impacted, as discussed in Sec. 4.2.2.

6 Summary and conclusions

This work assesses, for the first time, the detectability of the 21 cm signal as measured by the BINGO radiotelescope, in its Phase 1 of operation, through cross-correlation with galaxy catalogs. In particular, we explore the feasibility of using photometric surveys for this purpose, considering specifically here the future LSST survey, which presents an excellent overlap in area and redshift with BINGO. Cross-correlation between H_I IM and photometric surveys has not been deeply investigated due to poor photo- z constraints, with a clear preference in the literature for spectroscopic measurements. However, given the large number of current, high-quality, photometric surveys available, we believe that their synergy with H_I IM surveys should be better evaluated. Here, we explicitly show how photo- z errors would impact the cross-correlation measurements, focusing on employing the full photometric galaxy distribution (Fig. 1).

This is a novel approach, where we cross-correlate each of the 30 BINGO z -bins with the three LSST photo- z bins, in a complementary fashion of what is presented, e.g., in [39], where the photometric galaxies are selected to match the H_I bin width. Our analyses employ the APS as a clustering estimator, suitable in the case of pixelized line intensity maps, and rely on BINGO-like and LSST-like simulations. We analyze the sky region delimited by the BINGO footprint (fully covered by LSST), investigating also the impact of including thermal noise and foreground residuals. In contrast with results from [39], we do not find a significant degradation of the cross-correlation signal, on average, likely because considering the full photometric redshift bin increases the number of galaxies also contributing to the H_I signal.

However, we observe that the 68% region from the APS calculated from simulations is wider for cross-correlation compared to autocorrelation, which we suspect is due to the photo- z error. To investigate this point, we implemented a null test, in which we cross-correlate a H_I map with a set of Gaussian random maps, mimicking the presence of galaxies in the photometric sample not contributing to the H_I signal. This test indicates that such galaxies introduce a noise-like behavior in the cross-APS, explaining why the auto-APS shows a higher SNR. Additionally, it is interesting to notice from our results that such behavior is similar to the impact from adding thermal noise and foregrounds residuals, which also boost the noise in auto and cross-correlation.

However, since the H_I contaminants do not correlate with the galaxies, no bias is observed in the average amplitude of the cross-APS. On the other hand, for H_I autocorrelation, although the 68% regions are smaller, a clear bias is found at larger multipoles, whose amplitude and affected multipoles vary with the redshift bin. Based on our study of the SNR from both auto and cross-APS, we selected the highest SNR multipole range to assess the statistical significance of the APS detection. We find that, given the noise-like behavior introduced by the photo- z error, the statistical significance of the cross-correlation from H_I bins closest to the center of the photo- z distribution is reduced to levels comparable to that from autocorrelation.

In fact, the significance gets smaller the further away is the z -bin from the center of the galaxy distribution. This is expected, given that the number of galaxies contributing to both tracers gets smaller the farther the H_I bin is from the center of the photo- z distribution, decreasing the amplitude of the expected cross-APS and increasing the noise at the same time.

Finally, considering the same multipole range, we also evaluate how well actual BINGO observations would provide constraints on the degenerate quantities $b_{\text{H I}} \Omega_{\text{H I}}$ and $b_{\text{H I}} \Omega_{\text{H I}} r$ from auto and cross-correlation, respectively. We find that the autocorrelation should bias the estimates towards higher redshifts, where the foreground residual is more relevant. From cross-correlation, considering only the cross-APS that could be detected according to our statistical significance analysis, no bias is observed. However, the constrained values are impacted by the photo- z error and the presence

of contaminants, showing a noise-like behavior, with a larger 1σ dispersion of the estimated values compared to results from autocorrelation. Still, both auto and cross-correlation results indicate that constraints would be possible, considering the semi realistic simulations considered here.

It is worth emphasizing that, while our analysis brings new findings to the context of using cross-correlation to detect the H α signal and the use of photometric surveys for this task, the synergy between BINGO and LSST deserves further study. Accounting for effects from beam shape, $1/f$ noise, and polarization leakage, should have a more significant impact on autocorrelation. Also, a thinner slicing of the BINGO frequency band, that is, a larger number of z -bins, would also contribute to a better performance of the foreground cleaning process, allowing to improve auto- and cross-APS estimates. Therefore, our results suggest that the refinement of the current analyses, in the light of real data, should produce very interesting results.

Another interesting aspect we plan to investigate in future analyses is the possibility of improving the SNR from cross-correlations by combining the H α z -bins encompassed by the photometric galaxy distribution. Summing all the radio redshift bins inside a given photo- z interval might increase the likelihood of detecting the H α signal through cross-correlation with photometric surveys, presenting this method as an additional tool to be used for cross-correlation analyses.

Finally, we stress that even using BINGO-like and LSST-like simulations, which is not the most realistic scenario, our results indicate that the combination of current and future photometric and radio IM data have quite a good potential to detect the H α signal through cross-correlation. This motivates future investigation towards a more complete framework to assess the full capability of cross-correlating photometric galaxy surveys with H α IM experiments, BINGO and LSST being our best bet for the near future.

Acknowledgments

G.A.S.S. acknowledges resources received from CAPES under process 88887.602823/2021-00. C.P.N. thanks Serrapilheira Institute and São Paulo Research Foundation (FAPESP; grant 2019/06040-0) for financial support. C.A. Wuensche thanks CNPq for grants 407446/2021-4 and 312505/2022-1, the Brazilian Ministry of Science, Technology and Innovation (MCTI) and the Brazilian Space Agency (AEB) who supported the present work under the PO 20VB.0009. B.B.B. acknowledges resources received from FAPESP under processes 2021/04786-5, 2022/16749-0 and 2024/12902-3. E.J.M. thanks INPE for the financial support provided by the PCI fellowship. The authors thank V. Liccardo and R. Mokeddem for useful discussions and manuscript reading. The BINGO project is supported by FAPESP-PB, the State of Paraíba, FINEP, and FAPESP-SP, Brazil, by means of several grants. The results of this work used the software packages `astropy` [80], `healpy` [81], `numpy` [82], `scipy` [78], `matplotlib` [83], `UCLCℓ` [44] and `FLASK` [59].

References

- [1] B.E. Robertson, *Galaxy Formation and Reionization: Key Unknowns and Expected Breakthroughs by the James Webb Space Telescope*, *Ann. Rev. Astron. Astrophys.* **60** (2022) 121 [2110.13160].
- [2] L. Amendola, S. Appleby, A. Avgoustidis, D. Bacon, T. Baker, M. Baldi et al., *Cosmology and fundamental physics with the Euclid satellite*, *Living rev. relativ.* **21** (2018) 1.
- [3] Ž. Ivezić, S.M. Kahn, J.A. Tyson, B. Abel, E. Acosta, R. Allsman et al., *LSST: from science drivers to reference design and anticipated data products*, *The Astrophysical Journal* **873** (2019) 111.
- [4] X. Chen, *The tianlai project: a 21cm cosmology experiment*, in *Int. J. Mod. Phys. Conf. Ser.*, vol. 12, pp. 256–263, World Scientific, 2012.

- [5] D. Crichton, M. Aich, A. Amara, K. Bandura, B.A. Bassett, C. Bengaly et al., *Hydrogen intensity and real-time analysis experiment: 256-element array status and overview*, *J. Astron. Telesc. Instrum. Syst.* **8** (2022) 011019.
- [6] R. Nan, D. Li, C. Jin, Q. Wang, L. Zhu, W. Zhu et al., *The five-hundred-meter aperture spherical radio telescope (FAST) project*, *Int. J. Mod. Phys. D* **20** (2011) 989.
- [7] D.J. Bacon, R.A. Battye, P. Bull, S. Camera, P.G. Ferreira, I. Harrison et al., *Cosmology with phase 1 of the square kilometre array red book 2018: technical specifications and performance forecasts*, *Publications of the Astronomical Society of Australia* **37** (2020) e007.
- [8] R. Battye, I. Browne, C. Dickinson, G. Heron, B. Maffei and A. Pourtsidou, *HI intensity mapping: a single dish approach*, *Mon. Not. R. Astron. Soc.* **434** (2013) 1239.
- [9] M.-A. Bigot-Sazy, C. Dickinson, R.A. Battye, I. Browne, Y.-Z. Ma, B. Maffei et al., *Simulations for single-dish intensity mapping experiments*, *Mon. Not. R. Astron. Soc.* **454** (2015) 3240.
- [10] E. Abdalla, E.G. Ferreira, R.G. Landim, A.A. Costa, K.S. Fornazier, F.B. Abdalla et al., *The BINGO project-I. baryon acoustic oscillations from integrated neutral gas observations*, *Astron. Astrophys.* **664** (2022) A14.
- [11] M.G. Santos, M. Cluver, M. Hilton, M. Jarvis, G.I. Jozsa, L. Leeuw et al., *Meerklass: MeerKAT large area synoptic survey*, *arXiv preprint arXiv:1709.06099* (2017).
- [12] K. Bandura, G.E. Addison, M. Amiri, J.R. Bond, D. Campbell-Wilson, L. Connor et al., *Canadian hydrogen intensity mapping experiment (chime) pathfinder*, in *Ground-based and Airborne Telescopes V*, vol. 9145, p. 914522, SPIE, 2014.
- [13] M. Tegmark, A. de Oliveira-Costa and A.J.S. Hamilton, *High resolution foreground cleaned cmb map from wmap*, *Phys. Rev. D* **68** (2003) 123523.
- [14] D. Alonso, P. Bull, P.G. Ferreira and M.G. Santos, *Blind foreground subtraction for intensity mapping experiments*, *Mon. Not. R. Astron. Soc.* **447** (2015) 400.
- [15] L. Olivari, M. Remazeilles and C. Dickinson, *Extracting HI cosmological signal with generalized needlet internal linear combination*, *Mon. Not. R. Astron. Soc.* **456** (2016) 2749.
- [16] I.P. Carucci, M.O. Irfan and J. Bobin, *Recovery of 21-cm intensity maps with sparse component separation*, *Mon. Not. R. Astron. Soc.* **499** (2020) 304.
- [17] C.A. Wuensche, T. Villela, E. Abdalla, V. Liccardo, F. Vieira, I. Browne et al., *The BINGO project-II. instrument description*, *Astron. Astrophys.* **664** (2022) A15.
- [18] S. Harper, C. Dickinson, R. Battye, S. Roychowdhury, I. Browne, Y.-Z. Ma et al., *Impact of simulated 1/f noise for HI intensity mapping experiments*, *Mon. Not. R. Astron. Soc.* **478** (2018) 2416.
- [19] Y. Li, M.G. Santos, K. Grainge, S. Harper and J. Wang, *HI intensity mapping with MeerKAT: 1/f noise analysis*, *Mon. Not. R. Astron. Soc.* **501** (2021) 4344.
- [20] J. Ding, X. Wang, U.-L. Pen and X.-D. Li, *Correlation-based beam calibration of 21 cm intensity mapping*, *Astrophys. J. Supp.* **274** (2024) 44.
- [21] J. Wang, M.G. Santos, P. Bull, K. Grainge, S. Cunnington, J. Fonseca et al., *HI intensity mapping with MeerKAT: calibration pipeline for multidish autocorrelation observations*, *Mon. Not. R. Astron. Soc.* **505** (2021) 3698.
- [22] T.-C. Chang, U.-L. Pen, K. Bandura and J.B. Peterson, *An intensity map of hydrogen 21-cm emission at redshift $z \sim 0.8$* , *Nature* **466** (2010) 463.
- [23] E. Switzer, K. Masui, K. Bandura, L.-M. Calin, T.-C. Chang, X.-L. Chen et al., *Determination of $z \sim 0.8$ neutral hydrogen fluctuations using the 21 cm intensity mapping autocorrelation*, *Mon. Not. R. Astron. Soc.* **434** (2013) L46.
- [24] K. Masui, E. Switzer, N. Banavar, K. Bandura, C. Blake, L.-M. Calin et al., *Measurement of 21 cm brightness fluctuations at $z \sim 0.8$ in cross-correlation*, *Astrophys. J.* **763** (2013) L20.

- [25] L. Wolz, A. Pourtsidou, K.W. Masui, T.-C. Chang, J.E. Bautista, E.-M. Müller et al., *HI constraints from the cross-correlation of eBOSS galaxies and Green Bank Telescope intensity maps*, *Mon. Not. R. Astron. Soc.* **510** (2021) 3495.
- [26] S. Cunnington, Y. Li, M.G. Santos, J. Wang, I.P. Carucci, M.O. Irfan et al., *HI intensity mapping with meerkat: power spectrum detection in cross-correlation with wigglez galaxies*, *Mon. Not. R. Astron. Soc.* **518** (2023) 6262.
- [27] M. Amiri, K. Bandura, T. Chen, M. Deng, M. Dobbs, M. Fandino et al., *Detection of cosmological 21 cm emission with the canadian hydrogen intensity mapping experiment*, *Astrophys. J.* **947** (2023) 16.
- [28] S. Paul, M.G. Santos, Z. Chen and L. Wolz, *A first detection of neutral hydrogen intensity mapping on mpc scales at $z \approx 0.32$ and $z \approx 0.44$* , *arXiv preprint arXiv:2301.11943* (2023) .
- [29] S. Dodelson, *Modern cosmology*, Academic Press, Massachusetts, USA (2003).
- [30] Z. Gao, A. Raccanelli and Z. Vlah, *Asymptotic connection between full-and flat-sky angular correlators*, *Phys. Rev. D* **108** (2023) 043503.
- [31] I.P. Carucci, J.L. Bernal, S. Cunnington, M.G. Santos, J. Wang, J. Fonseca et al., *Hydrogen intensity mapping with meerkat: Preserving cosmological signal by optimising contaminant separation*, *arXiv preprint arXiv:2412.06750* (2024) .
- [32] C. Blake, *Power spectrum modelling of galaxy and radio intensity maps including observational effects*, *Mon. Not. R. Astron. Soc.* **489** (2019) 153.
- [33] S. Cunnington and L. Wolz, *Accurate fourier-space statistics for line intensity mapping: Cartesian grid sampling without aliased power*, *Mon. Not. R. Astron. Soc.* **528** (2024) 5586.
- [34] J.N. Benabou, I. Sands, H.S.G. Gebhardt, C. Heinrich and O. Doré, *Wide-angle effects in the power spectrum multipoles in next-generation redshift surveys*, *Phys. Rev. D* **110** (2024) 083526.
- [35] A. Pourtsidou, D. Bacon and R. Crittenden, *Cross-correlation cosmography with intensity mapping of the neutral hydrogen 21 cm emission*, *Phys. Rev. D* **92** (2015) 103506.
- [36] H. Padmanabhan, A. Refregier and A. Amara, *Impact of astrophysics on cosmology forecasts for 21 cm surveys*, *Mon. Not. R. Astron. Soc.* **485** (2019) 4060.
- [37] H. Padmanabhan, A. Refregier and A. Amara, *Cross-correlating 21 cm and galaxy surveys: implications for cosmology and astrophysics*, *Mon. Not. R. Astron. Soc.* **495** (2020) 3935.
- [38] F. Shi, Y.-S. Song, J. Asorey, D. Parkinson, K. Ahn, J. Yao et al., *Hir4: cosmological signatures imprinted on the cross-correlation between a 21-cm map and galaxy clustering*, *Mon. Not. R. Astron. Soc.* **499** (2020) 4613.
- [39] S. Cunnington, L. Wolz, A. Pourtsidou and D. Bacon, *Impact of foregrounds on HI intensity mapping cross-correlations with optical surveys*, *Mon. Not. R. Astron. Soc.* **488** (2019) 5452.
- [40] T. Abbott, F. Abdalla, A. Alarcon, S. Allam, F. Andrade-Oliveira, J. Annis et al., *Dark energy survey year 1 results: Measurement of the baryon acoustic oscillation scale in the distribution of galaxies to redshift 1*, *Mon. Not. R. Astron. Soc.* **483** (2019) 4866.
- [41] N. Benitez, R. Dupke, M. Moles, L. Sodre, J. Cenarro, A. Marin-Franch et al., *J-pas: the javalambre-physics of the accelerated universe astrophysical survey*, *arXiv preprint arXiv:1403.5237* (2014) .
- [42] C. Hikage, M. Oguri, T. Hamana, S. More, R. Mandelbaum, M. Takada et al., *Cosmology from cosmic shear power spectra with subaru hyper supprime-cam first-year data*, *Publ. of the Astr. Soc. Japan* **71** (2019) 43.
- [43] S. Serrano, E. Gaztañaga, F.J. Castander, M. Eriksen, R. Casas, D. Navarro-Gironés et al., *The physics of the accelerating universe survey: narrow-band image photometry*, *Monthly Notices of the Royal Astronomical Society* **523** (2023) 3287.

- [44] A. Loureiro, B. Moraes, F.B. Abdalla, A. Cuceu, M. McLeod, L. Whiteway et al., *Cosmological measurements from angular power spectra analysis of boss dr12 tomography*, *Mon. Not. R. Astron. Soc.* **485** (2019) 326.
- [45] L. Wolz, C. Tonini, C. Blake and J. Wyithe, *Intensity mapping cross-correlations: connecting the largest scales to galaxy evolution*, *Mon. Not. R. Astron. Soc.* **458** (2016) 3399.
- [46] F. Sobreira, F. de Simoni, R. Rosenfeld, L. da Costa, M. Maia and M. Makler, *Cosmological forecasts from photometric measurements of the angular correlation function*, *Phys. Rev. D* **84** (2011) 103001.
- [47] M. McLeod, S.T. Balan and F.B. Abdalla, *A joint analysis for cosmology and photometric redshift calibration using cross-correlations*, *Mon. Not. R. Astron. Soc.* **466** (2017) 3558.
- [48] J. Lesgourgues, *The cosmic linear anisotropy solving system (class) i: Overview*, *arXiv preprint arXiv:1104.2932* (2011) .
- [49] D. Blas, J. Lesgourgues and T. Tram, *The cosmic linear anisotropy solving system (CLASS). Part II: approximation schemes*, *J. Cosmol. Astropart. Phys.* **2011** (2011) 034.
- [50] D. Alonso, J. Sanchez, A. Slosar and L.D.E.S. Collaboration, *A unified pseudo-Cl framework*, *Mon. Not. R. Astron. Soc.* **484** (2019) 4127.
- [51] E. Hivon, K.M. Górski, C.B. Netterfield, B.P. Crill, S. Prunet and F. Hansen, *Master of the cosmic microwave background anisotropy power spectrum: a fast method for statistical analysis of large and complex cosmic microwave background data sets*, *Astrophys. J.* **567** (2002) 2.
- [52] E.J. Mericia, L.C. Santos, C.A. Wuensche, V. Liccardo, C.P. Novaes, J. Delabrouille et al., *Testing synchrotron models and frequency resolution in bingo 21 cm simulated maps using gnild*, *Astron. Astrophys.* **671** (2023) A58.
- [53] C.P. Novaes, J. Zhang, E.J. de Mericia, F.B. Abdalla, V. Liccardo, C.A. Wuensche et al., *The BINGO project-VIII. recovering the BAO signal in hi intensity mapping simulations*, *Astronomy & Astrophysics* **666** (2022) A83.
- [54] C.P. Novaes, E.J. de Mericia, F.B. Abdalla, C.A. Wuensche, L. Santos, J. Delabrouille et al., *Cosmological constraints from low redshift 21 cm intensity mapping with machine learning*, *Monthly Notices of the Royal Astronomical Society* **528** (2024) 2078.
- [55] Z. Zhang, C. Chang, P. Larsen, L.F. Secco, J. Zuntz and L.D.E.S. Collaboration, *Transitioning from stage-iii to stage-iv: cosmology from galaxy× cmb lensing and shear× cmb lensing*, *Mon. Not. R. Astron. Soc.* **514** (2022) 2181.
- [56] The LSST Dark Energy Science Collaboration, R. Mandelbaum, T. Eifler, R. Hložek, T. Collett, E. Gawiser et al., *The lsst dark energy science collaboration (desc) science requirements document*, 2021.
- [57] R.A. Shaw and M.A. Strauss, *LSST data challenge handbook - version 1*, 2011.
- [58] K.M. Gorski, E. Hivon, A.J. Banday, B.D. Wandelt, F.K. Hansen, M. Reinecke et al., *Healpix: A framework for high-resolution discretization and fast analysis of data distributed on the sphere*, *Astrophys. J.* **622** (2005) 759.
- [59] H.S. Xavier, F.B. Abdalla and B. Joachimi, *Improving lognormal models for cosmological fields*, *Mon. Not. R. Astron. Soc.* **459** (2016) 3693 [[1602.08503](#)].
- [60] J. Zhang, P. Motta, C.P. Novaes, F.B. Abdalla, A.A. Costa, B. Wang et al., *The BINGO project-VI. Hi halo occupation distribution and mock building*, *Astron. Astrophys.* **664** (2022) A19.
- [61] J. Dunkley, E. Komatsu, M. Nolta, D. Spergel, D. Larson, G. Hinshaw et al., *Five-year wilkinson microwave anisotropy probe* observations: likelihoods and parameters from the wmap data*, *Astrophys. J. Supp.* **180** (2009) 306.

- [62] V. Liccardo, E.J. de Mericia, C.A. Wuensche, E. Abdalla, F.B. Abdalla, L. Barosi et al., *The BINGO project-IV. simulations for mission performance assessment and preliminary component separation steps*, *Astron. Astrophys.* **664** (2022) A17.
- [63] K.S. Fornazier, F.B. Abdalla, M. Remazeilles, J. Vieira, A. Marins, E. Abdalla et al., *The bingo project-v. further steps in component separation and bispectrum analysis*, *Astron. Astrophys.* **664** (2022) A18.
- [64] J. Delabrouille, M. Betoule, J.-B. Melin, M.-A. Miville-Deschênes, J. Gonzalez-Nuevo, M. Le Jeune et al., *The pre-launch planck sky model: a model of sky emission at submillimetre to centimetre wavelengths*, *Astron. Astrophys.* **553** (2013) A96.
- [65] M. Remazeilles, C. Dickinson, A. Banday, M.-A. Bigot-Sazy and T. Ghosh, *An improved source-subtracted and destriped 408-mhz all-sky map*, *Mon. Not. R. Astron. Soc.* **451** (2015) 4311.
- [66] M.-A. Miville-Deschênes, N. Ysard, A. Lavabre, N. Ponthieu, J.-F. Macias-Perez, J. Aumont et al., *Separation of anomalous and synchrotron emissions using wmap polarization data*, *Astron. Astrophys.* **490** (2008) 1093.
- [67] C. Dickinson, R. Davies and R. Davis, *Towards a free-free template for cmb foregrounds*, *Mon. Not. R. Astron. Soc.* **341** (2003) 369.
- [68] P. Collaboration et al., *Planck 2015 results: Xxvi. the second planck catalogue of compact sources*, *Astron. Astrophys.* **594** (2016) A26.
- [69] J.L. Tinker, B.E. Robertson, A.V. Kravtsov, A. Klypin, M.S. Warren, G. Yepes et al., *The large-scale bias of dark matter halos: numerical calibration and model tests*, *Astrophys. J.* **724** (2010) 878.
- [70] F.B. Abdalla, A. Marins, P. Motta, E. Abdalla, R.M. Ribeiro, C.A. Wuensche et al., *The BINGO Project-III. optical design and optimization of the focal plane*, *Astron. Astrophys.* **664** (2022) A16.
- [71] M. Remazeilles, J. Delabrouille and J.-F. Cardoso, *CMB and SZ effect separation with constrained Internal Linear Combinations*, *Mon. Not. R. Astron. Soc.* **410** (2011) 2481 [[1006.5599](#)].
- [72] S. Cunnington, M.O. Irfan, I.P. Carucci, A. Pourtsidou and J. Bobin, *21-cm foregrounds and polarization leakage: cleaning and mitigation strategies*, *Mon. Not. R. Astron. Soc.* **504** (2021) 208.
- [73] L. Wolz, C. Blake and J. Wyithe, *Determining the h i content of galaxies via intensity mapping cross-correlations*, *Mon. Not. R. Astron. Soc.* **470** (2017) 3220.
- [74] L. Wolz, S. Murray, C. Blake and J. Wyithe, *Intensity mapping cross-correlations ii: Hi halo models including shot noise*, *Mon. Not. R. Astron. Soc.* **484** (2019) 1007.
- [75] Y.-E. Jiang, Y. Gong, M. Zhang, Q. Xiong, X. Zhou, F. Deng et al., *Cross-correlation forecast of csst spectroscopic galaxy and meerkat neutral hydrogen intensity mapping surveys*, *Research in Astronomy and Astrophysics* **23** (2023) 075003.
- [76] A. Mazumder, L. Wolz, Z. Chen, S. Paul, M. Santos, M. Jarvis et al., *HI intensity mapping with the MIGHTEE survey: First results of the HI power spectrum*, *arXiv preprint arXiv:2501.17564* (2025) .
- [77] J. Zheng, P. Tiwari, G.-B. Zhao, D.J. Schwarz, D. Bacon, S. Camera et al., *Cosmology from lofar two-metre sky survey data release 2: Cross-correlations with luminous red galaxies from eboss*, *arXiv preprint arXiv:2504.20722* (2025) .
- [78] P. Virtanen, R. Gommers, T.E. Oliphant and et al., *Scipy 1.0: Fundamental algorithms for scientific computing in python*, *Nat. Methods* **17** (2020) 261.
- [79] J. Hartlap, P. Simon and P. Schneider, *Why your model parameter confidences might be too optimistic. unbiased estimation of the inverse covariance matrix*, *Astron. Astrophys.* **464** (2007) 399.
- [80] A.M. Price-Whelan, B. Sipőcz, H. Günther, P. Lim, S. Crawford, S. Conseil et al., *The astropy project: building an open-science project and status of the v2. 0 core package*, *Astron. J.* **156** (2018) 123.

- [81] A. Zonca, L. Singer, D. Lenz, M. Reinecke, C. Rosset, E. Hivon et al., *healpy: equal area pixelization and spherical harmonics transforms for data on the sphere in python*, *J. Open Source Softw.* **4** (2019) 1298.
- [82] S. Van Der Walt, S.C. Colbert and G. Varoquaux, *The numpy array: a structure for efficient numerical computation*, *Computing in science & engineering* **13** (2011) 22.
- [83] J.D. Hunter, *Matplotlib: A 2d graphics environment*, *Comput. Sci. Eng.* **9** (2007) 90.